Progress In Electromagnetics Research M, Vol. 86, 59–69, 2019

Thermal Characteristics Analysis of Single-Winding Bearingless Switched Reluctance Motor

Yonghong Huang[1, *], Fengxiao Huang[1], Ying Zhang[2], Chi Chen[1], Ye Yuan[1], and Jianhua Luo[3]

Abstract—Loss and temperature rise are important parameters for performance evaluation of bearingless switched reluctance machine. In this paper, a 12/8 outer-rotor single-winding bearingless switched reluctance motor (SWBSRM) is studied for its loss and temperature rise under high speed operation. Firstly, a 2D finite element model is established by using Ansoft Maxwell, and the magnetic flux density waveform and the variation law of different parts of the core are obtained. Furthermore, various losses including core loss and copper loss are coupled to the temperature field analysis module as a heat source. Thirdly, the thermal model is established by Motor-CAD, and the transient and stable temperature field is simulated and analyzed. Finally, the temperature field distributions of the core and windings are obtained.

1. INTRODUCTION

Bearingless switched reluctance motors (BSRM), with the advantages of simple structure, excellent fault-tolerant capability, no mechanical loss, are suitable for flywheel energy storage, aerospace, and other fields [1–4]. BSRM generates losses including copper loss, core loss, and other losses during operation, resulting in temperature rise, and excessive temperature will not only reduce the efficiency of the motor, but also accelerate the insulation of the winding and reduce the service life [5–8]. In order to ensure efficient and reliable operation, it is important to analyze the loss and temperature rise of BSRM.

At present, there are few studies on loss calculation and temperature analysis of BSRM. The research of BSRM loss and thermal analysis can be largely referred to the SRM research method, for the great similarity between BSRM and SRM, which both adopt the double salient pole structure and only the stator wound with windings [9, 10]. Reference [11] studies the core loss characteristics of BSRM and uses improved Steinmetz equation to calculate core loss. Reference [12] uses a fast and accurate method to calculate the loss and efficiency of 16/12 pole BSRM under different working conditions and verifies it by finite element method and experiment. This method is suitable for high power density and wide speed range motors in the traction field. Reference [13] proposes a calculation method for the copper loss of SRM, which has obvious advantages in optimizing the winding configuration. Reference [14] analyzes the thermal characteristics of SRM under different working conditions. It is concluded that under high vacuum conditions, the temperature of each component is about twice as high as that under natural cooling conditions, and the average temperature of rotor is higher than the stator. Reference [15] performs the thermal analysis of a 24/16 motor by using Motor-CAD software and determines the heat distribution within the motor.

Received 23 July 2019, Accepted 24 September 2019, Scheduled 23 October 2019

* Corresponding author: Yonghong Huang (hyh@ujs.edu.cn).

[1] School of Electrical and Information Engineering, Jiangsu University, Zhenjiang 212013, China. [2] Nantong Power Supply Company, Jiangsu Province, China. [3] Yanchen Power Supply Company, Jiangsu Province, China.

In this paper, a 12/8 outer-rotor single-winding bearingless switched reluctance motor (SWBSRM) is studied for its loss and temperature rise under high speed operation. In Section 2, the finite element analysis (FEA) is used to analyze the variation of magnetic flux density at the special position of the stator and rotor, and verifies the core loss results. The heat loss such as copper loss and stray loss of the motor are also calculated. In Section 3, the equivalent thermal conductivity and convection coefficient of the motor are analyzed. In Section 4, the thermal analysis model is established by Motor-CAD, the temperature distribution of motor under rated operation and the change of temperature of the motor with time are obtained. Finally, the conclusions are given in Section 5.

2. LOSS ANALYSIS

2.1. Loss Calculation Model

The solution of the motor temperature field is inseparable from the heat source, which is related to losses generated by the motor during operation. So the accurate calculation of the loss is the premise of calculating the temperature field. In this paper, the temperature field of 12/8 outer-rotor SWBSRM under high speed operation is studied. The structure, cross section, and its main parameters of the motor are shown in Figure 1 and Table 1, respectively. The loss of outer-rotor SWBSRM mainly includes core loss, copper loss, and additional loss, and the total loss can be expressed as

$$P = P_{Cu} + P_{Fe} + P_s \tag{1}$$

where P is the total loss; P_{Fe} is the core loss; P_{Cu} is the copper loss; P_s is the additional loss.

Table 1. Design parameters of SWBSRM.

Types	Value	Types	Value
Rated power (kW)	1.2	Air-gap length (mm)	0.25
Rated speed (rpm)	13000	Axial length (mm)	40
Rotor outside diameter (mm)	130	Stator tooth arc (degree)	15
Rotor inside diameter (mm)	97.5	Rotor tooth arc (degree)	16
Stator inside diameter (mm)	37	Number of coil turns	32
Stator yoke thickness (mm)	11	Rotor yoke thickness (mm)	9

When the outer-rotor SWBSRM is operating in a steady state, the copper loss of the winding is proportional to the square of the effective value of the winding current. The calculation formula is as follows

$$P_{Cu} = mI_{\text{rms}}^2 R_{\text{phase}} \tag{2}$$

where I_{rms} is the effective value of winding current, R_{phase} the resistance of each phase winding, and m the number of phases.

Generally, additional loss is difficult to calculate with an accurate formula. In actual calculation, it is approximated by 6% of the total loss [16], which is as follows

$$P_s = (P_1 - P_2) \times 6\% \tag{3}$$

where P_1 is the input power, and P_2 is the output power.

The core loss in SWBSRM is one of the main losses. Especially when the motor is running at high speed, the core loss is especially obvious. At present, Bertotti model [17] is applied to the calculation of core loss. It is pointed out that the core loss is divided into three components: hysteresis loss, eddy current loss, and excess loss. It is worth noting that the model has been widely used, and many scholars have derived many improved models based on this theory. Under the condition of ignoring the skin effect, the calculation formula of the core loss per unit weight of silicon steel sheet under sinusoidal alternating magnetic field is as follows

$$P_{\text{Fe}} = P_h + P_c + P_e \tag{4}$$

where P_h, P_c, and P_e are the hysteresis loss, eddy-current loss, and excess loss, respectively.

$$P_h = \sum_{i=1}^{n} k_h \cdot f \cdot \left[B_{tm}^2 \cdot \left(1 + c \cdot \frac{1}{B_{rm}} \sum_{i=1}^{N} \Delta B_{ti} \right) + B_{rm}^2 \cdot \left(1 + c \cdot \frac{1}{B_{rm}} \sum_{i=1}^{N} \Delta B_{ri} \right) \right] \tag{5}$$

$$P_c = \sum_{i=1}^{n} k_c \cdot (if)^2 \cdot (B_{ri}^2 + B_{ti}^2) \tag{6}$$

$$P_e = \sum_{i=1}^{n} k_e \cdot (if)^{1.5} \cdot (B_{ri}^{1.5} + B_{ti}^{1.5}) \tag{7}$$

where k_h, k_c, and k_e are the coefficients of hysteresis loss, eddy-current loss, and excess loss, respectively; f is the fundamental frequency; i is the harmonic order; c is a constant, generally taking $c = 0.65$; B_{ti} and B_{ri} are amplitude of the tangential and radial magnetic flux density at the i time, respectively; B_{tm} and B_{rm} are the maximum value of the tangential and radial magnetic flux density at the i time, respectively.

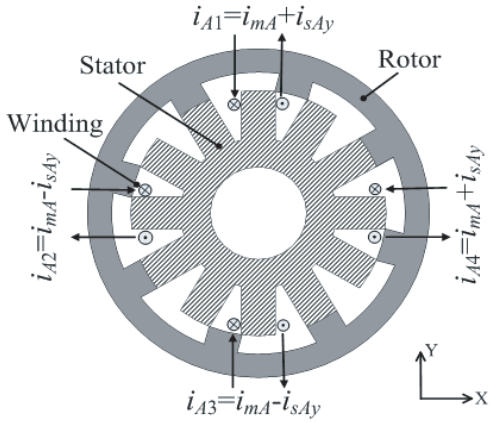

Figure 1. Structure and cross section of outer-rotor BSRM.

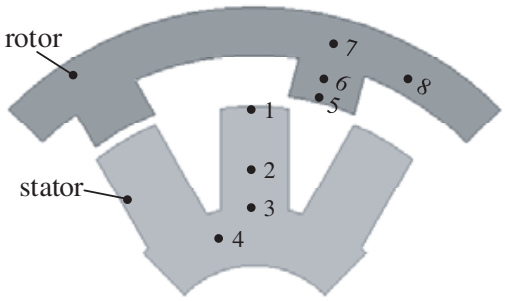

Figure 2. Location for the analysis of flux density.

2.2. Core Magnetic Density Analysis

From Equations (5), (6), (7), it can be found that the calculation of core loss is largely dependent on the magnetic field characteristics. It is necessary to first analyze the waveform and variation of the magnetic flux. At rated speed, the stator core material has been selected, and the frequency remains basically the same. The loss of the motor is mainly determined by the tangential and radial magnetic

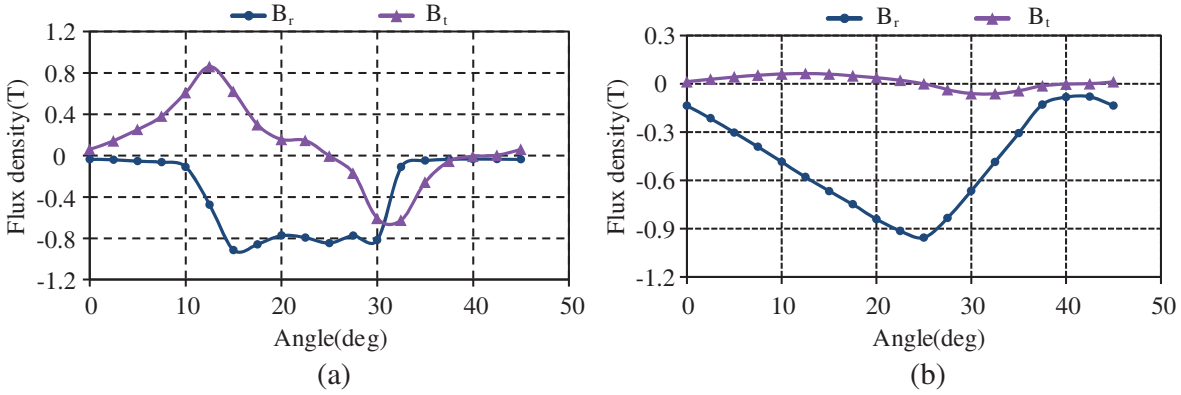

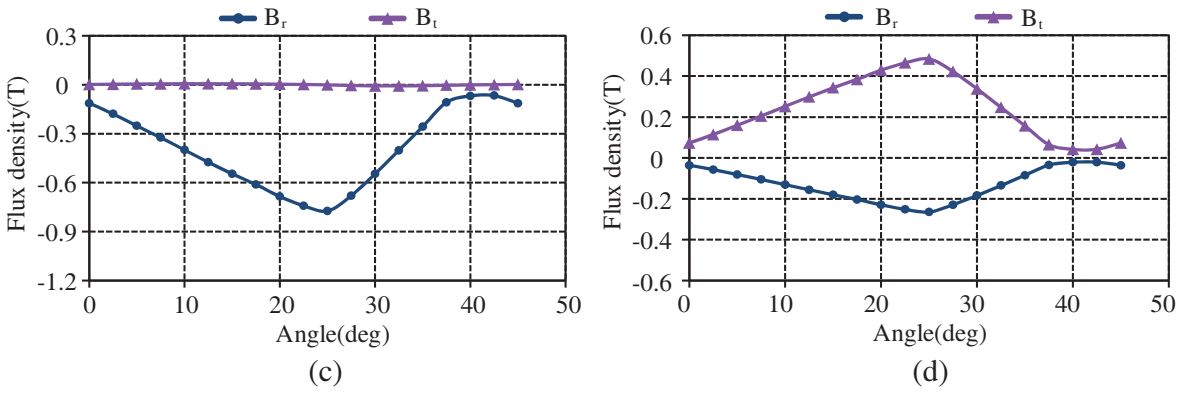

Figure 3. Variations of magnetic flux density on the stator, (a) point 1, (b) point 2, (c) point 3, (d) point 4.

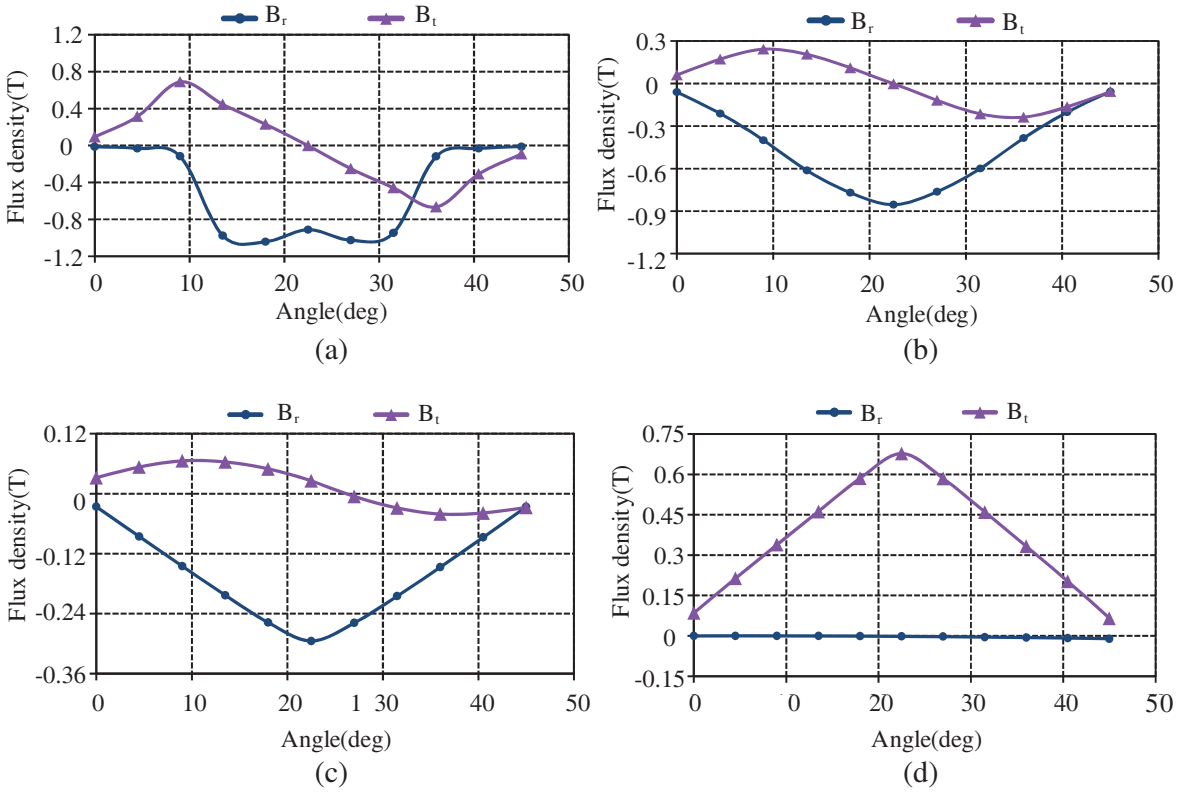

Figure 4. Variations of magnetic flux density on the rotor, (a) point 5, (b) point 6, (c) point 7, (d) point 8.

densities. Therefore, in order to accurately calculate the core loss of the outer-rotor SWBSRM, it is necessary to study the magnetic field distribution and variation of each part in the rotor core of the motor. Figure 2 shows some special position points to observe the change of the magnetic density.

Figure 3 shows B_r and B_t diagrams of point 1 (stator pole tip), point 2 (stator pole), point 3 (stator pole root), and point 4 (stator yoke), where B_t is the tangential magnetic density, and B_r is the radial magnetic density. It can be seen from Figure 3(a) that point 1 has the largest magnetic density amplitude, because the magnetic field lines basically pass through the air gap from the stator pole tip to the rotor core to form a closed path. Point 1 contains components B_r and B_t. The curve of B_r is saddle-shaped and remains substantially unchanged between 15° and 30°. The curve of B_t is a

triangular waveform and reaches a positive maximum at 12.5°. Comparing Figure 3(b) with Figure 3(c), the shapes of the magnetic-tight waveforms of point 2 and point 3 are substantially the same. However, point 2 contains a small amount of B_t, while point 3 has almost no B_t. As shown in Figure 3(d), point 4 has both components B_r and B_t, and their absolute values increase first and then decrease with the angle.

Figure 4 shows the B_r and B_t diagrams of point 5 (rotor pole tip), point 6 (rotor pole), point 7 (rotor tooth yoke junction), and point 8 (rotor yoke). From Figure 4(a), point 5 contains components B_r and B_t, which is similar to waveform of point 1. Comparing Figure 4(b) with Figure 4(c), the shapes of the magnetic dense waveforms of point 6 and point 7 are substantially the same. The curve of B_r is a triangular waveform, while B_t approximates a sinusoidal waveform. As shown in Figure 4(d), point 8 has only B_t with no B_r, and the value of B_t increases first and then decreases with the angle.

2.3. FEA Verification of Core Loss

In this section, FEA is used to verify the core loss. Figure 5 presents the core loss density distributions of the motor at different rotor positions. It can be found that the distributions of core loss density are different due to different distributions of magnetic lines of the core at different positions. Figure 6 shows the stator and rotor core loss distributions at a rated speed of 13000 r/min. It can be seen that the stator core loss is significantly larger than the rotor core loss, and its value is 137.28 W, wherein the hysteresis loss and eddy current loss are 126.21 W and 11.07 W, respectively. The core loss of the rotor is 101.77 W, wherein the hysteresis loss and eddy current loss are 95.16 W and 6.61 W, respectively. In

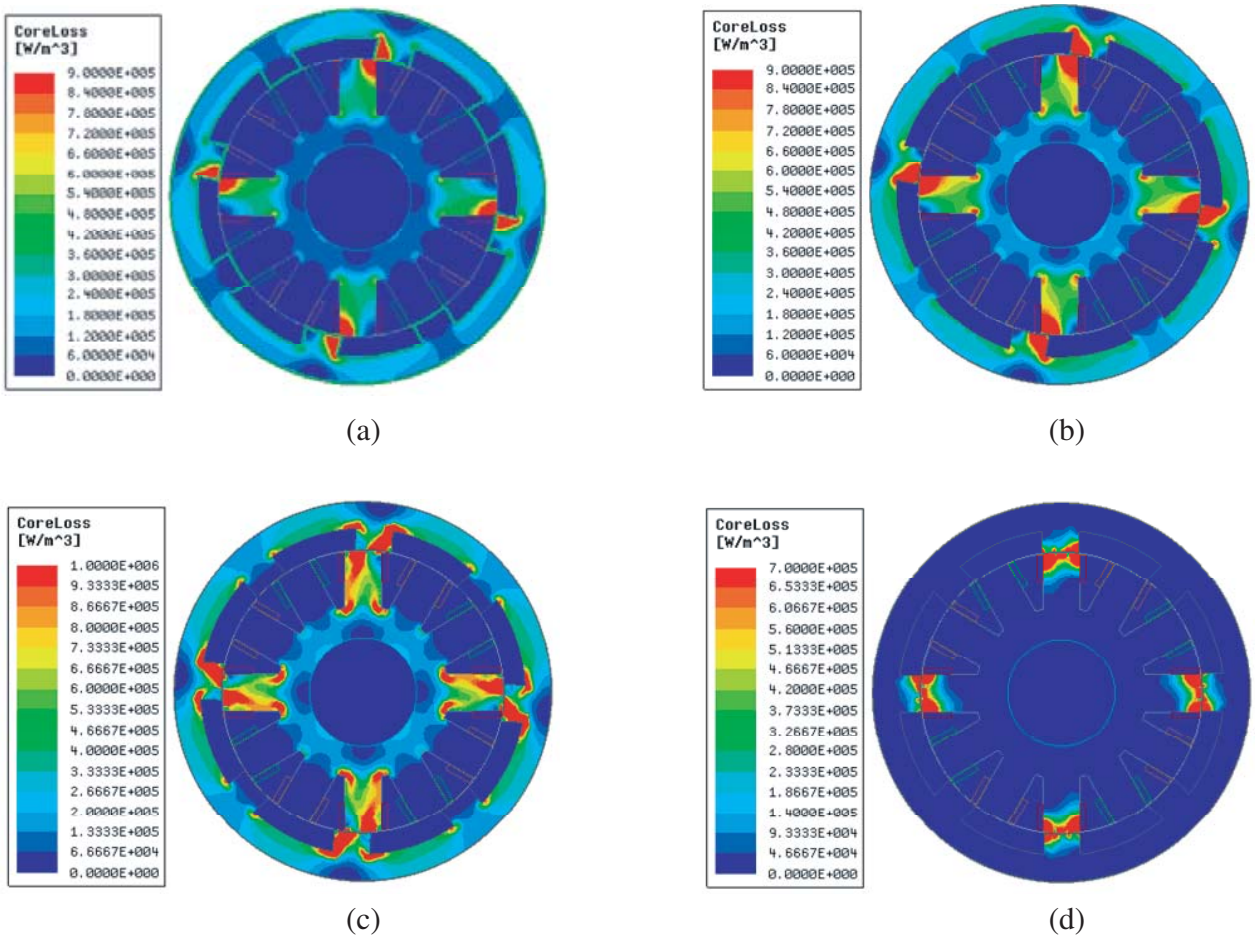

Figure 5. Distribution of iron loss density in different locations, (a) $\theta =$°, (b) $\theta = 3.6$°, (c) $\theta = 10.8$°, (d) $\theta = 15.3$°.

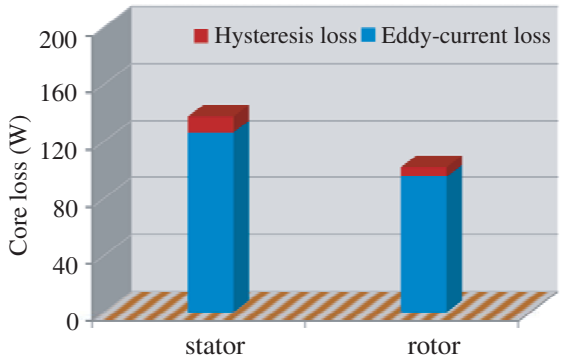

Figure 6. Core loss of SWBSRM.

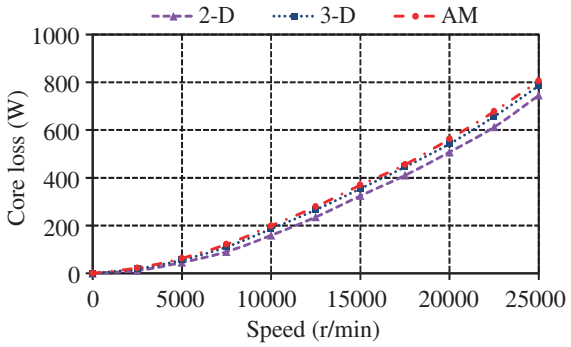

Figure 7. Core loss of SWBSRM with speed curve.

addition, from the above figure analysis, the eddy current loss is the main component of the outer-rotor SWBSRM core loss.

Figure 7 presents the variation of core loss with rotation speed. It can be found that the core loss increases with the increase of rotational speed. In addition, it is worth noting that the results of the analytical method are consistent with the 3-D simulation results and trends, and both are larger than the 2-D results, but acceptable within the error range, which verifies the correctness of the analytical method. The loss values of outer-rotor SWBSRM are listed in Table 2.

Table 2. Loss values of SWBSRM.

Types	Value
Copper loss (W)	18.23
Stator loss (W)	137.28
Rotor loss (W)	101.77
Additional loss (W)	19.09

3. TEMPERATURE FIELD PARAMETERS

In this section, the important parameters of the motor temperature field will be analyzed, paving the way for subsequent simulation.

3.1. Equivalent Thermal Conductivity

The thermal conductivity of outer-rotor SWBSRM mainly includes the equivalent thermal conductivity of the windings and core. The winding is simplified and considered as an equivalent part, so the equivalent thermal conductivity of the winding (λ_{eq}) is expressed as follows

$$\lambda_{eq} = \lambda_{cu} F_{ew} + \lambda_{imp}(1 - F_{ew}) \tag{8}$$

where λ_{cu} and λ_{imp} are the thermal conductivity of copper and insulating materials, respectively; F_{ew} is the slot full rate.

The core thermal conductivity can be equivalent to the heat conduction between the two layers. The formula for calculating the thermal conductivity of the iron core (k) is expressed

$$k = \frac{\Delta x_a + \Delta x_b}{\Delta x_a / k_a + \Delta x_a / k_b} \tag{9}$$

Table 3. Thermal properties of electrical materials.

Materials	Density (kg/m^3)	Heat capacity (J/kg/K)	Thermal conductivity (W/m/K)
Aluminum	2790	833	168
Silicon-steel sheets	7650	460	30
Copper	8933	385	401
Air	1.225	1006.43	0.0242

where Δx_a and Δx_b are the thicknesses of the first plate and second plate, respectively; k_a and k_b are the thermal conductivity of the first plate and second plate. Table 3 shows the thermal parameters of the motor material for thermal analysis of the outer-rotor SWBSRM.

The heat transfer between the stator and rotor is achieved by convection and heat conduction of the intermediate air gap medium. The concept of equivalent thermal conductivity is introduced in this paper. It uses the thermal conductivity of the stationary fluid to equivalently describe the heat transfer capacity of the flowing medium in the air gap, that is, the heat transferred by the stationary fluid between the stator and the rotor per unit time is the same as the heat transferred by the fluid. The formula for calculating the equivalent thermal conductivity of air gap is as follows

$$\lambda_{eff} = 0.23\left(\frac{\delta}{R_r}\right)^{0.25}\beta \mathrm{Re}^{0.5}\lambda_k \tag{10}$$

where λ_{eff} is the equivalent thermal conductivity of air gap; λ_k is the thermal conductivity of the air gap medium; β is the empirical coefficient; R_r is the outer diameter of the rotor; Re is the Reynolds number; δ is the air gap length.

3.2. Convection Coefficient

The surface convection coefficient of each part needs to be calculated when solving the temperature distribution of the motor. The convective heat transfer boundary condition of the outer-rotor SWBSRM is

$$\begin{cases} -k\dfrac{\partial T}{\partial t}\Big|_b = h_1(T_b - T_x) \\ -k\dfrac{\partial T}{\partial t}\Big|_b = h_2(T_b - T_x) \end{cases} \tag{11}$$

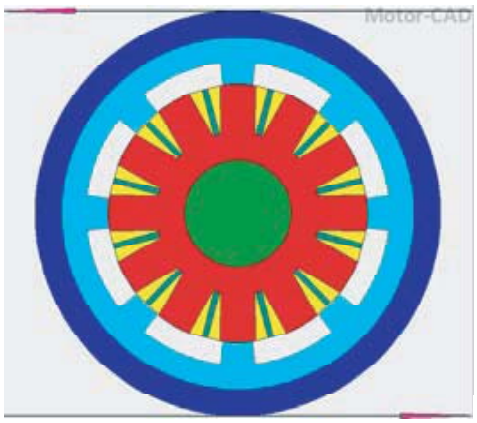

Figure 8. Thermal model.

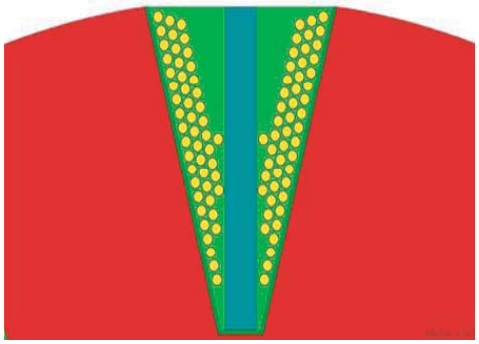

Figure 9. Winding configuration diagram.

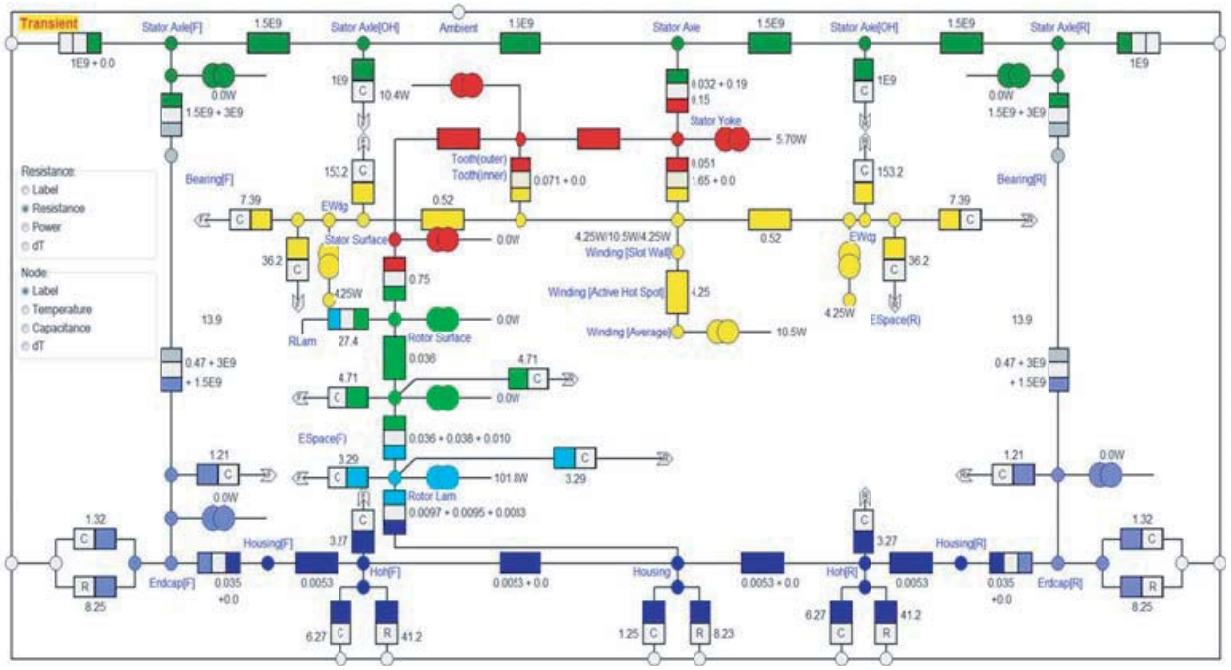

Figure 10. Equivalent thermal resistance of thermal network in Motor-CAD.

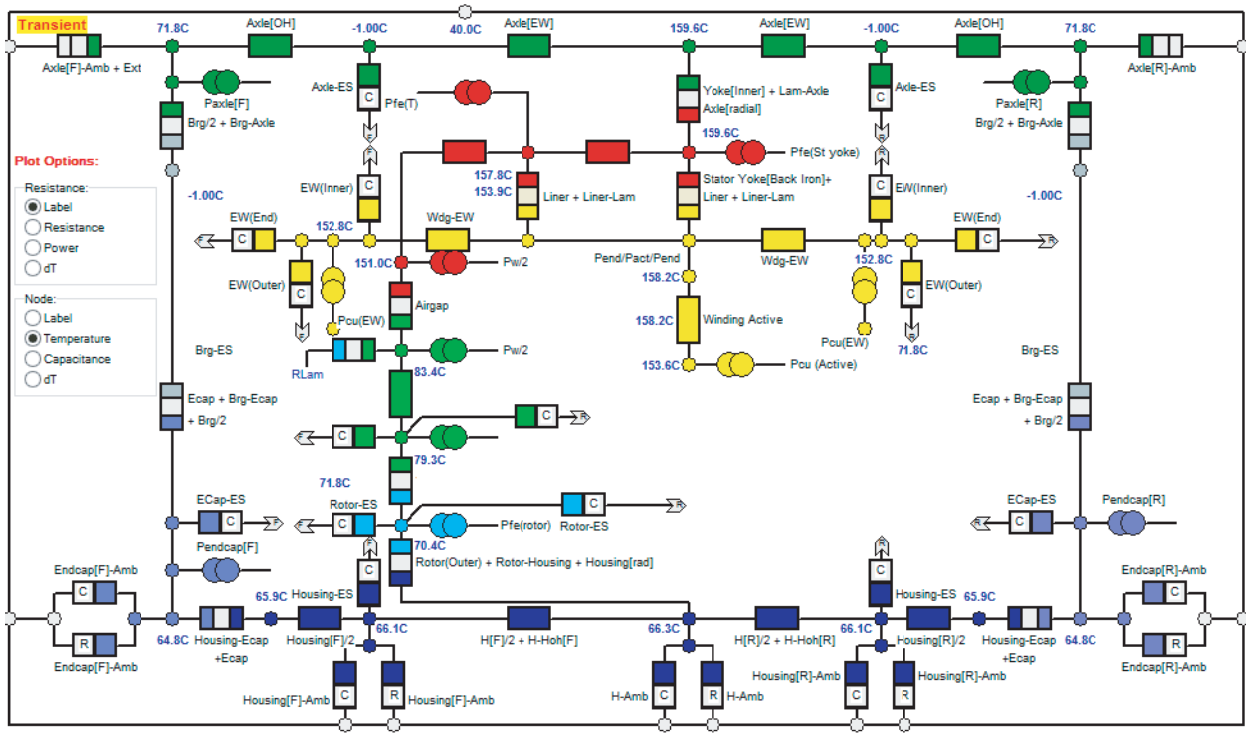

Figure 11. Default lumped parameter thermal network in Motor-CAD.

where h_1 and h_2 are the external and internal convective heat transfer coefficients of the motor, respectively; T_b is the surface temperature of the motor; T_x is the temperature of the air.

4. THERMAL SIMULATION AND ANALYSIS

In this section, Motor-CAD thermal analysis software is used to analyze the temperature of the outer-rotor SWBSRM. The thermal path method is used to analyze the temperature of the motor. The thermal analysis model is built in Motor-CAD based on the geometry of the outer-rotor SWBSRM prototype, as shown in Figure 8. The winding in Motor-CAD uses 32 strands of AWG30.5 wire with a slot fill factor of 0.57. The position of the wire is left at the default setting, as shown in Figure 9.

The equivalent thermal resistance and the temperature distribution of the outer-rotor SWBSRM thermal network are shown in Figures 10 and 11, respectively. Each node in the thermal network represents a specific spatial location on the motor geometry and is connected to other nodes based on the calculated thermal resistance value. It is worth noting that the thermal resistance value is calculated based on the motor size and material characteristics. All parts of the heat path are combined to form a thermal circuit system for the entire motor. Finally, the temperature distribution will change with the heat source, thermal network layout, and thermal resistance.

Figure 12 shows the temperature profile ($t = 140$ s) of the outer-rotor SWBSRM during short-term operation under natural air-cooling conditions. It can be found that the temperature of the motor shell is minimum when working for a short time; the temperature of the rotor teeth is slightly higher than that of the rotor yoke; the temperatures of stator pole tip, stator pole, stator yoke are about 63.0°C, 64.4°C, 64.0°C, respectively. Figure 13 shows the steady-state temperature distribution of the outer-rotor SWBSRM under natural air-cooling conditions. It can be seen that the highest temperature of the motor appears in stator windings, due to the small thermal conductivity of winding insulating medium, poor heat dissipation capability and a large amount of copper loss generated by windings.

Figure 14 shows the dynamics of stator, rotor and winding temperatures as a function of running

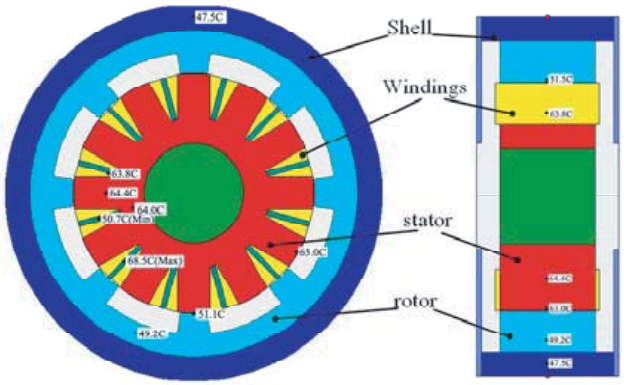

Figure 12. Temperature distribution at 140 s.

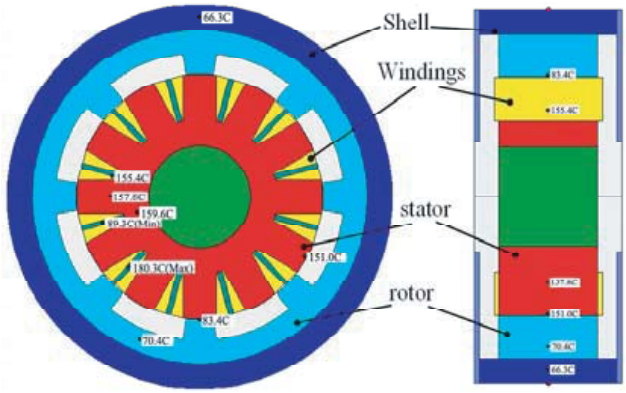

Figure 13. Temperature distribution at stable time.

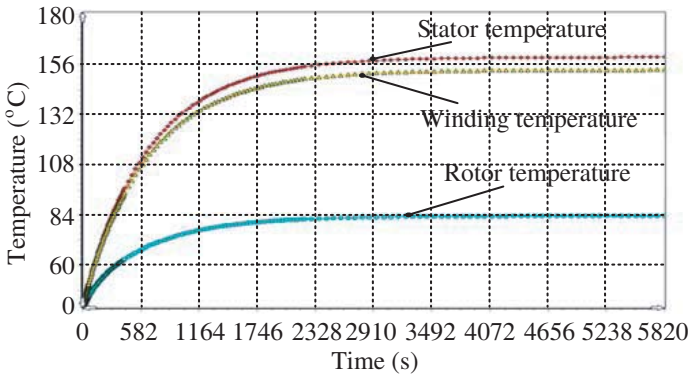

Figure 14. Temperature distribution.

time. It can be seen that the motor temperature increases rapidly with the running time, then increases slowly and tends to stabilize after 50 s. When the time is short, the temperature is proportional to the time. When the motor running time is greater than 2328 s, the temperature of the motor tends to be constant. It can be seen that the average temperature of the stator is the highest; the average temperature of the rotor is the lowest; and the average temperature of the winding is slightly lower than the average temperature of the stator.

5. CONCLUSION

In this paper, a 12/8 outer-rotor SWBSRM has been studied for its loss and temperature rise under high speed operation. A 2-D finite element model is established by using Ansoft Maxwell. By analyzing the magnetic flux density waveform of the stator and rotor, it is concluded that the core loss is mainly distributed on the teeth of stator and rotor, and the coreloss of yoke is relatively small. Then the loss of motor is coupled to the temperature field analysis module as a heat source. The thermal model is established by Motor-CAD. The temperature field distribution of the core and windings is obtained, which can provide a theoretical basis for the design of BSRM under high speed operation.

ACKNOWLEDGMENT

This work was supported in part by the National Natural Science Foundation of China under Project 51707082 and Project 51877101, by Natural Science Foundation of Jiangsu Province of China (Grants NO. BK20170546), and by the Priority Academic Program Development of Jiangsu Higher Education Institutions (PAPD).

REFERENCES

1. Chen, L. and W. Hofmann, "Speed regulation technique of one bearingless 8/6 switched reluctance motor with simpler single winding structure," *IEEE Transactions on Industrial Electronics*, Vol. 59, No. 6, 2592–2600, 2012.
2. Zhang, J., H. Wang, L. Chen, et al., "Multi-objective optimal design of bearingless switched reluctance motor based on multi-objective genetic particle swarm optimizer," *IEEE Transactions on Magnetics*, Vol. 54, No. 1, 1–13, 2018.
3. Sun, Y., Y. Yuan, and Y. Huang, "Design and analysis of bearingless flywheel motor specially for flywheel energy storage," *Electronics Letters*, Vol. 52, No. 1, 66–68, 2016.
4. Sun, Y., Y. Huang, and Y. Yuan, "Radial force dynamic current compensation method of single winding bearingless flywheel motor," *IET Power Electronics*, Vol. 8, No. 7, 1224–1229, 2015.
5. Garcia-Amoros, J., P. Andrada, B. Blanque, et al., "Influence of design parameters in the optimization of linear switched reluctance motor under thermal constraints," *IEEE Transactions on Industrial Electronics*, Vol. 65, No. 2, 1875–1883, 2018.
6. Toda, H., K. Senda, S. Morimoto, et al., "Influence of various non-oriented electrical steels on motor efficiency and iron loss in switched reluctance motor," *IEEE Transactions on Magnetics*, Vol. 49, No. 7, 3850–3853, 2013.
7. Yan, W., H. Chen, X. Liu, et al., "Design and multi-objective optimisation of switched reluctance machine with iron loss," *IET Electric Power Applications*, Vol. 13, No. 4, 435–444, 2019.
8. Chen, H., Y. Xu, and H. C. Iu, "Analysis of temperature distribution in power converter for switched reluctance motor drive," *IEEE Transactions on Magnetics*, Vol. 48, No. 2, 991–994, 2012.
9. Dev, C. M., A. Firdausa, K. Gaurav, et al., "Design methodology for a special single winding based bearingless switched reluctance motor," *The Journal of Engineering*, Vol. 2017, No. 7, 274–284, 2017.
10. Cao, X., H. Yang, L. Zhang, et al., "Compensation strategy of levitation forces for single-winding bearingless switched reluctance motor with one winding total short-circuited," *IEEE Transactions on Industrial Electronics*, Vol. 63, No. 9, 5534–5546, 2016.

11. Liu, J., X. Zhang, H. Wang, et al., "Iron loss characteristic for the novel bearingless switched reluctance motor," *2013 International Conference on Electrical Machines and Systems (ICEMS)*, 586–591, IEEE, 2013.
12. Yu, Q., B. Bilgin, and A. Emadi, "Loss and efficiency analysis of switched reluctance machines using a new calculation method," *IEEE Transactions on Industrial Electronics*, Vol. 62, No. 5, 3072–3080, 2015.
13. Al Eit, M., P. Dular, and F. Bouillault, "Perturbation finite element method for efficient copper losses calculation in switched reluctance machines," *IEEE Transactions on Magnetics*, Vol. 53, No. 6, 7202004, 2017.
14. Sun, Y., B. Zhang, Y. Yuan, and F. Yang, "Thermal characteristics of switched reluctance motor under different working conditions," *Progress In Electromagnetics Research M*, Vol. 74, 11–23, 2018.
15. Kasprzak, M., et al., "Thermal analysis of a three-phase 24/16 switched reluctance machine used in HEVs," *IEEE Energy Conversion Congress and Exposition*, 1–7, 2017.
16. Raulin, V., A. Radun, and I. Husain, "Modeling of losses in switched reluctance machines," *IEEE Transactions on Industry Applications*, Vol. 40, No. 6, 1560–1569, 2004.
17. Boivie, J., "Iron loss model and measurements of the losses in a switched reluctance motor," *International Conference on Electrical Machines & Drives, IET*, 219–222, 1993.